



January 2012

A High Energy X-Ray Diffraction Investigation Of Sodium Phosphate Glasses Doped With Less Than 5 Mol% Praseodymium Oxides

Kailing Zhang

Follow this and additional works at: <https://commons.und.edu/theses>

Recommended Citation

Zhang, Kailing, "A High Energy X-Ray Diffraction Investigation Of Sodium Phosphate Glasses Doped With Less Than 5 Mol% Praseodymium Oxides" (2012). *Theses and Dissertations*. 1389.
<https://commons.und.edu/theses/1389>

This Thesis is brought to you for free and open access by the Theses, Dissertations, and Senior Projects at UND Scholarly Commons. It has been accepted for inclusion in Theses and Dissertations by an authorized administrator of UND Scholarly Commons. For more information, please contact zeinebyousif@library.und.edu.

A HIGH ENERGY X-RAY DIFFRACTION INVESTIGATION OF SODIUM
PHOSPHATE GLASSES DOPED WITH LESS THAN 5 MOL% PRASEODYMIUM
OXIDES

by

Kailing Zhang
Bachelor of Science, Beijing Jiaotong University - China, 2010

A Thesis

Submitted to the Graduate Faculty

of the

University of North Dakota

in partial fulfillment of the requirements

for the degree of

Master of Science

Grand Forks, North Dakota
December 2012

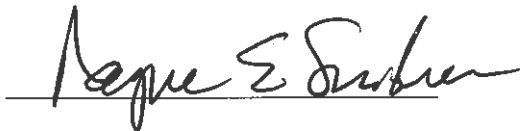
This thesis, submitted by Kailing Zhang in partial fulfillment of the requirements for the degree of Master of Science from the University of North Dakota, has been read by the Faculty Advisory Committee under whom the work has been done and is hereby approved.



Chairperson



This thesis meets the standards for appearance, conforms to the style and format requirements of the Graduate School of the University of North Dakota, and is hereby approved.



Dean of the Graduate School



Date

PERMISSION

Title A high energy X-ray diffraction investigation of sodium phosphate glasses doped with less than 5 mol% praseodymium oxides

Department Physics and Astrophysics

Degree Master of Science

In presenting this thesis in partial fulfillment of the requirements for a graduate degree from the University of North Dakota, I agree that the library of this University shall make it freely available for inspection. I further agree that permission for extensive copying for scholarly purposes may be granted by the professor who supervised my thesis work or, in his absence, by the chairperson of the department or the dean of the Graduate School. It is understood that any copying or publication or other use of this thesis or part thereof for financial gain shall not be allowed without my written permission. It is also understood that due recognition shall be given to me and to the University of North Dakota in any scholarly use which may be made of any material in my thesis.

Signature Kailing Zhang

Date December 5 2012

TABLE OF CONTENTS

LIST OF FIGURES	v
LIST OF TABLES	vii
ABSTRACT	viii
CHAPTER	
I. INTRODUCTION	1
II. EXPERIMENTAL	8
2.1 An Overview of The High Energy X-ray Diffraction Technique	8
2.2 Theory of High Energy X-ray Diffraction Technique	8
2.3 Preparation of REPGs	12
2.4 Data Collection	14
2.5 Methods of HEXRD Data Analysis	17
III. RESULTS AND DISCUSSION	25
3.1 Results	25
3.2 Discussion	33
IV. CONCLUSION	40
REFERENCES	42

LIST OF FIGURES

Figure	Page
1. Electronic energy levels and observed absorption, emission transitions of praseodymium ions.	2
2. Emission spectra of $(\text{Nd}_2\text{O}_3)_x(\text{Na}_2\text{O})_y(\text{P}_2\text{O}_5)_{1-x-y}$ glasses with different compositions....	5
3. Area of emission lines shown in Figure 2 vs. x of $(\text{Nd}_2\text{O}_3)_x(\text{Na}_2\text{O})_y(\text{P}_2\text{O}_5)_{1-x-y}$ glasses	6
4. Elastic scattering in reciprocal space..	9
5. Praseodymium doped sodium phosphate glasses.	13
6. Ternary plot showing the batched composition of $(\text{Pr}_2\text{O}_3)_x(\text{Na}_2\text{O})_y(\text{P}_2\text{O}_5)_{1-x-y}$ glasses in this study.....	14
7. Polyimide tubes containing powder samples	15
8. HEXRD setup at beamline 11-ID-C.	16
9. Sketch of the HEXRD experimental setup shown in Figure 8	16
10. Averaged 2D high energy X-ray diffraction patterns for (a) $(\text{Pr}_2\text{O}_3)_{0.005}(\text{Na}_2\text{O})_{0.395}(\text{P}_2\text{O}_5)_{0.6}$ (b) $(\text{Pr}_2\text{O}_3)_{0.01}(\text{Na}_2\text{O})_{0.39}(\text{P}_2\text{O}_5)_{0.6}$	18
11. Averaged 2D high energy X-ray diffraction patterns for (c) $(\text{Pr}_2\text{O}_3)_{0.02}(\text{Na}_2\text{O})_{0.38}(\text{P}_2\text{O}_5)_{0.6}$ (d) $(\text{Pr}_2\text{O}_3)_{0.03}(\text{Na}_2\text{O})_{0.37}(\text{P}_2\text{O}_5)_{0.6}$	19
12. Averaged 2D high energy X-ray diffraction patterns for (e) $(\text{Pr}_2\text{O}_3)_{0.04}(\text{Na}_2\text{O})_{0.36}(\text{P}_2\text{O}_5)_{0.6}$ (f) $(\text{Pr}_2\text{O}_3)_{0.05}(\text{Na}_2\text{O})_{0.35}(\text{P}_2\text{O}_5)_{0.6}$	20
13. Flow chart for Fit-2D program.	21
14. Intensity vs. 2θ plots for $(\text{Pr}_2\text{O}_3)_x(\text{Na}_2\text{O})_y(\text{P}_2\text{O}_5)_{1-x-y}$ glasses.	22
15. Flow chart for the analysis of HEXRD data for praseodymium-doped sodium phosphate glasses	23
16. Dependence of mass density on rare earth oxide content for $(\text{Pr}_2\text{O}_3)_x(\text{Na}_2\text{O})_y(\text{P}_2\text{O}_5)_{1-x-y}$ glasses.	25

17. X-ray structure factors, $S(Q)$, for $(\text{Pr}_2\text{O}_3)_x(\text{Na}_2\text{O})_y(\text{P}_2\text{O}_5)_{1-x-y}$ glasses	26
18. Pair distribution function $G(r)$ for $(\text{Pr}_2\text{O}_3)_x(\text{Na}_2\text{O})_y(\text{P}_2\text{O}_5)_{1-x-y}$ glasses	27
19. $G(r)$ for $(\text{Pr}_2\text{O}_3)_{0.05}(\text{Na}_2\text{O})_{0.35}(\text{P}_2\text{O}_5)_{0.6}$ glasses (dotted line) fitted with Gaussians.	28
20. Comparison of $G(r)$ for KZPr050 glass sample with inter-atomic distance distribution of crystalline $\text{NdNaP}_4\text{O}_{12}$	29
21. Emission spectra of Pr-Na-P-O glasses with different praseodymium concentrations	30
22. Integrated area of the emission line at ~640 nm vs. x for $(\text{Pr}_2\text{O}_3)_x(\text{Na}_2\text{O})_y(\text{P}_2\text{O}_5)_{1-x-y}$ glasses.....	31
23. $G(r)$ for $(\text{Pr}_2\text{O}_3)_x(\text{Na}_2\text{O})_y(\text{P}_2\text{O}_5)_{1-x-y}$ glasses (dotted line) with $x=0.005, 0.01, 0.02$ fitted with Gaussians	34
24. $G(r)$ for $(\text{Pr}_2\text{O}_3)_x(\text{Na}_2\text{O})_y(\text{P}_2\text{O}_5)_{1-x-y}$ glasses (dotted line) with $x=0.03, 0.04, 0.05$ fitted with Gaussians	35
25. The effect of composition on the Pr-O coordination number for $(\text{Pr}_2\text{O}_3)_x(\text{Na}_2\text{O})_y(\text{P}_2\text{O}_5)_{1-x-y}$ glasses.	37
26. The effect of composition on the Pr-O inter-atomic distances for $(\text{Pr}_2\text{O}_3)_x(\text{Na}_2\text{O})_y(\text{P}_2\text{O}_5)_{1-x-y}$ glasses.	38
27. Integrated area of selected emission lines vs. x for $(\text{Pr}_2\text{O}_3)_x(\text{Na}_2\text{O})_y(\text{P}_2\text{O}_5)_{1-x-y}$ (left) and $(\text{Nd}_2\text{O}_3)_x(\text{Na}_2\text{O})_y(\text{P}_2\text{O}_5)_{1-x-y}$ (right) glasses.	39

LIST OF TABLES

Table	Page
1. Frequently used laser-active ions, host glasses and emission wavelengths.	1
2. Performance comparison of phosphate laser glasses with silicate and fluoride laser glasses.	3
3. Batched compositions and densities of $(\text{Pr}_2\text{O}_3)_x(\text{Na}_2\text{O})_y(\text{P}_2\text{O}_5)_{1-x-y}$ glasses.	13
4. Coordination numbers N_{ij} and inter-atomic distances r_{ij} (Å) of $(\text{Pr}_2\text{O}_3)_x(\text{Na}_2\text{O})_y(\text{P}_2\text{O}_5)_{1-x-y}$ glasses obtained by fitting $G(r)$ s.	32

ABSTRACT

Rare earth phosphate glasses (REPGs) are excellent materials for high energy (10^3 - 10^6 J) / high peak power (10^{12} - 10^{15} W) lasers. Previous work of the rare earth doped sodium phosphate glasses with compositions $(R_2O_3)_x(Na_2O)_y(P_2O_5)_{1-x-y}$ where R= Nd, Eu and Dy, $0.04 < x < 0.13$ showed that the intensity of the emission spectra increases with decreasing R_2O_3 content. In this study, praseodymium doped sodium phosphate glasses with even lower praseodymium oxide concentrations, $(Pr_2O_3)_x(Na_2O)_y(P_2O_5)_{1-x-y}$, where $0.005 < x < 0.05$ were processed and characterized focusing on the region where the lasing efficiency is possibly going to peak. Emission spectra for the glass samples were measured to study how the florescence efficiency change with Pr^{3+} concentration. High Energy X-ray diffraction technique was used to study the atomic-scale structure of the rare-earth doped sodium phosphate glass samples. Structural features such as inter-atomic distances, coordination numbers and their dependence on the concentration of the rare-earth oxides were gained from analyzing pair distribution functions extracted from diffraction data.

CHAPTER I

INTRODUCTION

Rare-earth doped glasses are some of the most popular solid-state optical gain media. The most frequently used laser-active rare earth ions and host media, together with typical emission wavelength ranges are given in Table 1 [1]. Because this study focuses on praseodymium-doped glasses, energy levels and laser transitions of praseodymium ions are shown in Fig 1 [2].

Table 1. Frequently used laser-active ions, host glasses and emission wavelengths.

Rare earth ion	Common host glasses	Important emission wavelengths
Neodymium (Nd ³⁺)	Silicate and phosphate glasses	1.03-1.1 μ m, 0.9-0.95 μ m, 1.32-1.35 μ m
Ytterbium (Yb ³⁺)	Silicate glass	1.0-1.1 μ m
Erbium (Er ³⁺)	Silicate and phosphate glasses, fluoride glasses	1.5-1.6 μ m, 2.7 μ m, 0.55 μ m
Thulium (Tm ³⁺)	Silicate and germanate glasses, fluoride glasses	1.7-2.1 μ m, 1.45-1.53 μ m, 0.48 μ m, 0.8 μ m
Praseodymium (Pr ³⁺)	Silicate and fluoride glasses	1.3 μ m, 0.635 μ m, 0.6 μ m, 0.52 μ m, 0.49 μ m
Holmium (Ho ³⁺)	Silicate glasses, fluorozirconate glasses	2.1 μ m, 2.9 μ m

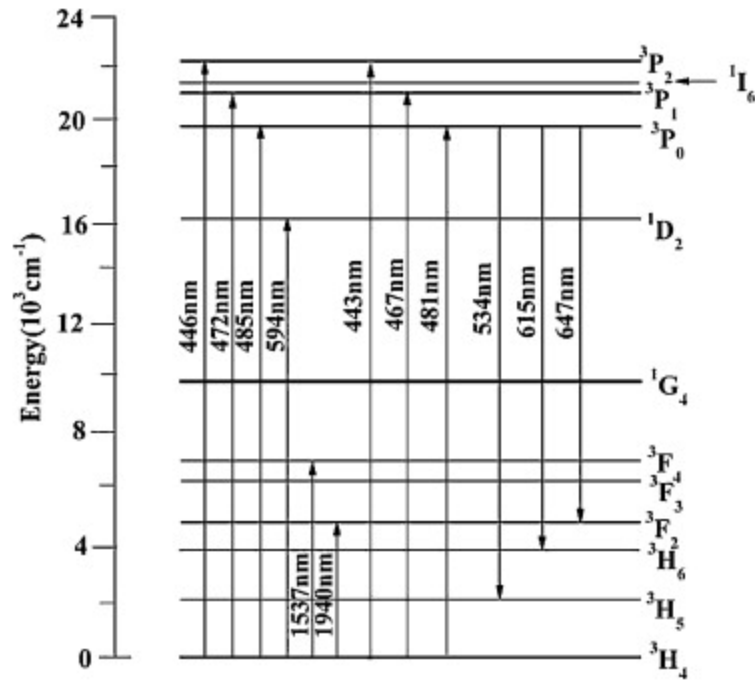


Figure 1. Electronic energy levels and observed absorption, emission transitions of praseodymium ions.

Compared to other host media for laser-active rare earth ions, almost every aspect of the phosphate glass offers an advantage for producing optimized high energy ($10^3 - 10^6$ J) / high peak power ($10^{12} - 10^{15}$ W) lasers (table below). Phosphate glasses, which are frequently used in the form of bulk or optical fibers, possess a series of interesting properties such as low glass transition temperature (T_g), lower melting temperature (compared to silicate glass), high thermal expansion coefficient and bio-compatibility. They are finding ever-increasing applications in fusion energy research, material processing, spectroscopy, medical surgery and communications etc.

Table 2. Performance comparison of phosphate laser glasses with silicate and fluoride laser glasses [3].

Host Material	Rare-Earth Solubility	Up-conversion	Dopant Level	Gain	Length
Silica	Low	High	<1000ppm	Lower	Long
Fluoride	Middle	High	Middle	Low	Long
Phosphate	High	Lowest	High	High	Short

In rare earth phosphate glasses (REPGs), rare earth ions modify physical properties of the host, the P_2O_5 glass, by changing the P_4 structural network via the formation of cross-linked bonds. Rare earth ions force some of the bridging oxygens (-P-O-P type) to be converted to terminal (-P-O⁻) oxygens [4].

Because rare earth ions (R^{3+}) are the lasing centers, one would expect that a high concentration of R^{3+} yields increased lasing action in REPGs. In reality, however, this is not the case. In fact, the distances between the nearest R^{3+} ions and the coordination environment of R^{3+} ions play rather complex roles in determining the lasing efficiency of REPGs [5] [6].

Previous studies have suggested that the lasing action decreases when the distance between near-neighbor R^{3+} ions become relatively small, that is, when REPGs has higher R^{3+} ions concentrations. Short nearest R-R distances also severely impair the magnetic properties of REPGs [7]. This is due to concentration quenching, a phenomenon that limits the population of an excited state by unwanted effects such as cross relaxation and excitation migration, etc. In this process, the lifetime of electronic levels of R^{3+} ions is significantly reduced, resulting in a decrease of the overall fluorescence intensity in the gain media.

The problem pertaining to quenching has led scientists to focus on REPGs with lower R^{3+} concentrations. Consequently, rare earth ultraphosphate (REUP) glasses with rare earth molar fraction (x) less than 0.25 became a potential candidate for the next generation laser materials. Relatively longer near-neighbor R^{3+} - R^{3+} distances have made concentration quenching less prevalent in REUP glasses. However, the hygroscopic nature of ultraphosphates due to the relatively large fraction of P_2O_5 makes preparation of REUPs of desired low rare-earth concentration extremely difficult. One way to solve this problem was to add Na_2O as a “filler” [4]. Hence, in this study, a series of rare earth sodium phosphate glasses with varying R^{3+} concentrations have been investigated.

Previous work done by our group [4] includes a study of rare earth doped sodium phosphate glasses with compositions $(R_2O_3)_x(Na_2O)_y(P_2O_5)_{1-x-y}$ where $R= Nd, Eu$ or Dy and $x \sim 0.04$ to 0.13 . Figure 2 shows emission spectra of the neodymium doped sodium phosphate glasses from this study.

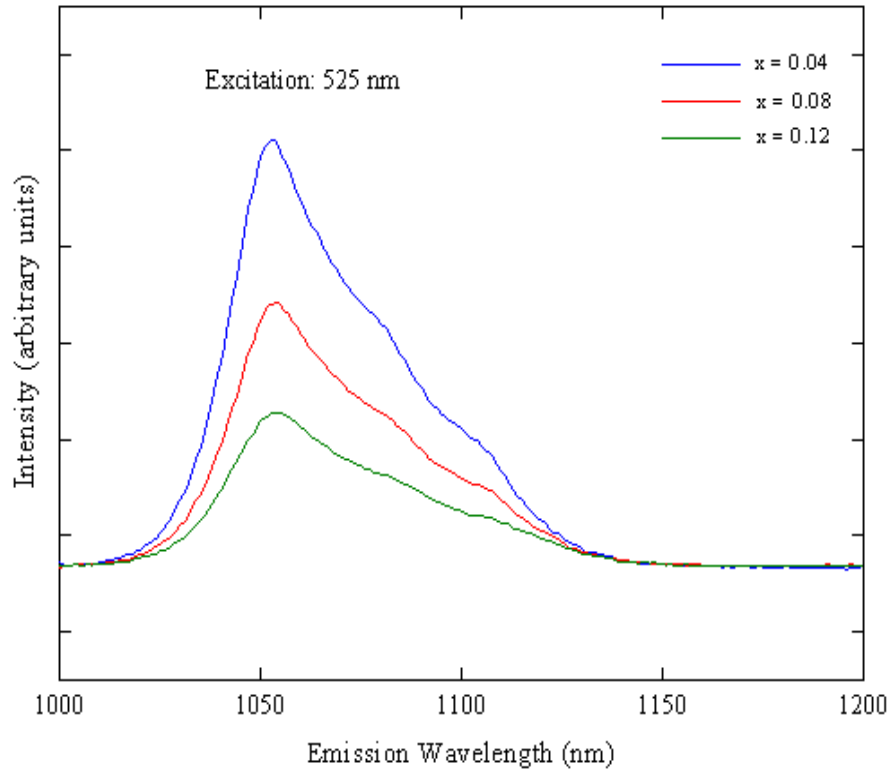


Figure 2. Emission spectra of $(\text{Nd}_2\text{O}_3)_x(\text{Na}_2\text{O})_y(\text{P}_2\text{O}_5)_{1-x-y}$ glasses with different compositions [4].

As seen in Figure 2 for neodymium sodium phosphate glasses, even at very low RE concentration ($x \sim 0.04$ to 0.13), the emission intensity increases with decreasing R_2O_3 content. This is most likely due to a decrease in concentration quenching. Figure 3 is a plot of integrated area under emission spectra shown in Figure 2 vs. molar fraction of Nd_2O_3 (x). We can easily see from this graph that the fluorescence performance increases with decreasing Nd_2O_3 composition. Continuing previous research, rare earth sodium phosphate glasses with even lower rare earth oxide concentration were investigated in this study, focusing on the region where the lasing efficiency may possibly reach its maximum.

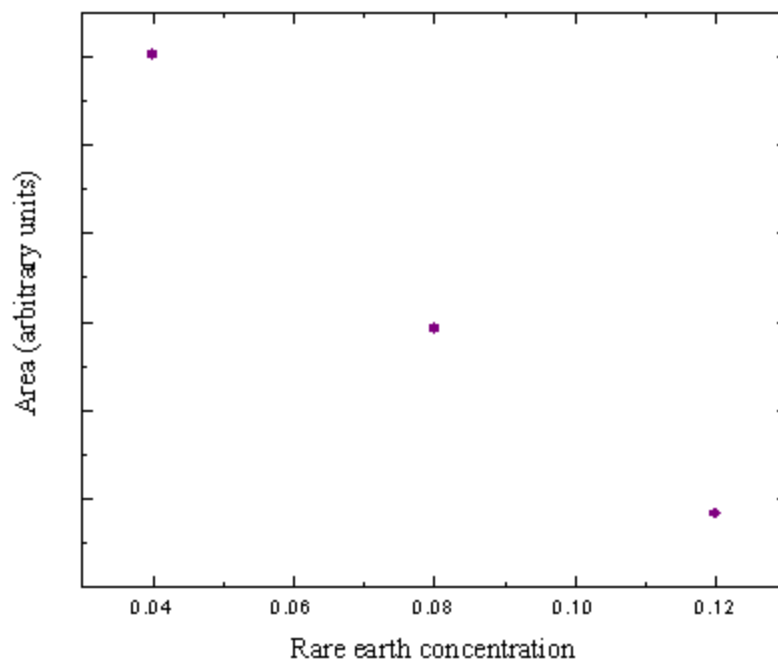


Figure 3. Area of emission lines shown in Figure 2 vs. x of $(\text{Nd}_2\text{O}_3)_x(\text{Na}_2\text{O})_y(\text{P}_2\text{O}_5)_{1-x-y}$ glasses

The coordination environment of rare earth ions, and consequently the electronic configuration of glass structure, has a profound effect on the luminescent properties of REPGs. For example, an irregular distribution of R^{3+} on lattice sites or occupancy of R^{3+} on defect sites randomizes the Stark splitting, while ion immiscibility causes clustering or precipitating of R^{3+} within domains [8]. These effects result in R^{3+} losing their lasing efficiency. In another example, line-widths of the $\text{Eu}^{3+} {}^5\text{D}_0 \rightarrow {}^7\text{F}_0$ transition [9] in several oxide glasses were compared and studied. The narrowest lines were found in the phosphate glasses, suggesting a relaxation of glass network forming more uniform environments around the modifier Eu^{3+} cations. Therefore, gaining information on the local atomic structure of the R^{3+} provides important insight on improving the optical properties of oxide materials in opto-electronic devices, through engineering R^{3+} coordination environment.

For most crystalline materials, knowledge of their long-range, periodic atomic structure is obtained using traditional Bragg X-ray diffraction. By measuring and analyzing the positions and intensities of Bragg diffraction peaks, we can determine the spatial characteristics of the crystal grating. It is difficult to use this approach on non-crystalline materials that do not show lattice periodicity, i.e. liquids or glasses, because their lack of Bragg scattering feature. However, a specialized combination of High Energy X-ray Diffraction (HEXRD) and atomic Partial Distribution Function (PDF) data analysis can be used to successfully tackle this problem [10].

In this study, praseodymium sodium phosphate glasses with nominal compositions $(\text{Pr}_2\text{O}_3)_x(\text{Na}_2\text{O})_y(\text{P}_2\text{O}_5)_{1-x-y}$, $0.005 < x < 0.05$ were prepared. HEXRD and PDF technique [11] were used to analyze the diffuse (non-Bragg type) X-ray diffraction patterns and obtain information such as nearest neighbor atomic distances and coordination numbers.

CHAPTER 2

EXPERIMENTAL

2.1 An Overview of The High Energy X-ray Diffraction Technique

HEXRD has its origin in the 1980's, with the pioneering work of Egelstaff who used γ -ray diffraction to obtain the structure factors of liquids [12]. In the mid 90's, Poulsen and Neufeld [13] adapted this technique to synchrotron radiation using 100 keV x-rays. Since then, HEXRD has become one of the primary techniques for material structural study.

There are mainly two advantages when hard X-rays (X-rays of energy in the vicinity of 100 keV) are used to study non-crystalline materials [12] [13]: (1) the structure factors can be measured out to much higher momentum transfers, $Q > 20 \text{\AA}^{-1}$ at small scattering angles, leading to higher real-space resolution, hence all the important details in the atomic-scale structure of a samples are revealed, (2) attenuation and multiple scattering effects are negligible for small samples [13] [14]. This is because the photo-electrical absorption decreases as $\sim E^{-3}$ and scattering becomes the dominant process.

2.2 Theory of High Energy X-ray Diffraction Technique

The scattering event in HEXRD is characterized by an energy transfer $\hbar\omega = E_o - E$ and a momentum transfer $\hbar\vec{Q} = \hbar\vec{k}_o - \hbar\vec{k}_1$. Wave vector \vec{Q} is defined as

$$Q = \frac{4\pi}{\lambda} \sin\theta, \quad (2.1)$$

where 2θ is the scattering angle and λ is the wavelength.

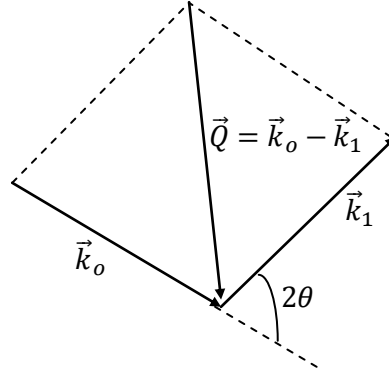


Figure 4. Elastic scattering in reciprocal space. For elastic scattering $|\vec{k}_0| = |\vec{k}_1|$.

The outcome of any scattering measurement is expressed in terms of the scattering cross-section σ . The differential cross-section is defined as the ratio of the scattered flux per unit solid angle (at large distances from the scattering center) to the incident flux.

$$\frac{d\sigma}{d\Omega} = \frac{\frac{\text{\# of photons scattered}}{\text{second}} \text{ towards the detector into a solid angle } d\Omega}{\Phi d\Omega} \quad (2.2)$$

where the flux Φ is the number of incident photons per second per unit cross-sectional area of the incident beam.

A master expression for the interpretation of scattering experiments is the partial differential cross-section which gives the fraction of photons of incident energy E scattered into an element of solid angle $d\Omega$ and with energy between E' and $E' + dE'$. The partial differential cross-section is denoted by $d^2\sigma/d\Omega dE'$ and has the dimension of area/energy.

Total scattering cross-section is given by

$$\sigma_{total} = \int_{all\ direction} \left(\frac{d\sigma}{d\Omega} \right) d\Omega. \quad (2.3)$$

The partial differential cross-section for coherent X-ray scattering is given by

$$\frac{d^2\sigma^{coh}}{d\Omega dE} = \frac{N_u a_e^2 k}{\hbar k_0} \sum_m \iint G_m(r, t) \exp^{i(\vec{Q}\cdot\vec{r} - \omega t)} dr dt, \quad (2.4)$$

where a_e is the scattering length, N_u is the number of scattering centers in a unit of composition in the sample and $G_m(r, t)$ is the electronic correlation function [4].

Above equation should be integrated over all energies using the static approximation that energy transfer is negligible ($k = k_0$ and $Q = Q_0$) and thus the intensity, $I_X^{coh}(Q)$, which is measured in HEXRD experiments, is written as

$$I_X^{coh}(Q) = \frac{1}{N_u} \frac{d\sigma^{coh}}{d\Omega} = a_e^2 \sum_m \int_0^\infty G_m(r, 0) e^{i\vec{Q}\cdot\vec{r}} dr. \quad (2.5)$$

The pseudonuclear static structure factor $S^X(Q)$ is the measured intensity corrected for background, polarization, attenuation, Compton and multiple scattering, absorption, detector geometry and other factors. It gives information about atomic interactions in the material, and can be Fourier-transformed into real space to yield the pair distribution function $G(r)$, which can be used to extract bond distances and local coordination numbers etc. $S^X(Q)$ is given by:

$$S^X(Q) = \frac{I_X(Q) - C_X(Q) - \sum_i f_i^2(Q)}{(\sum_i f_i(Q))^2}, \quad (2.6)$$

where $f_i(Q)$ is the electronic form factor for the i^{th} element and $C_X(Q)$ is the Compton scattering contribution.

The pair distribution correlation function $G(r)$ is obtained by Fourier transformation of $S^X(Q)$, provided a wide range of reciprocal space is covered [12]. $G(r)$ is written as

$$G(r) = 1 + \frac{1}{2\pi^2\rho_o} \int_0^{Q_{max}} M(Q)[S(Q) - 1]Q^2 \left(\frac{\sin(Qr)}{Qr}\right) dQ, \quad (2.7)$$

where ρ_o is the total number density of the glass sample. $M(Q)$ is an optional modification function. The only modification function used here is one due to Lorch ($r^* = \pi/Q_{max}$):

$$M(Q) = \frac{\sin(Q r^*)}{(Q r^*)}. \quad (2.8)$$

When performing the Fourier transform of $S^X(Q)$ to obtain $G(r)$, due to some premature cutoffs, truncation errors are introduced producing Fourier wiggles that interfere with peak resolution. To correct these errors to some extent, the window function $M(Q)$ is introduced when taking the Fourier transform.

The total real space correlation function, $T(r) = \sum W_{ij}T_{ij}(r)$, can be calculated from:

$$T(r) = 4\pi r\rho_o G(r) \quad (2.9)$$

and

$$T(r) = 4\pi r\rho_o + \frac{2}{\pi} \int_0^{Q_{max}} M(Q)[S(Q) - 1]Q \sin(Qr) dQ. \quad (2.10)$$

W_{ij} are weighting factors which depend on concentration and scattering power of the atom species:

$$W_{ij} = \frac{c_i c_j f_i(Q=0) f_j(Q=0)}{(c_O f_O(Q=0) + c_P f_P(Q=0) + c_{Na} f_{Na}(Q=0) + c_R f_R(Q=0))^2}, \quad (2.11)$$

where c_i is the concentration of the neighboring atom species. The radial distribution function $N(r)$ is given by

$$N(r) = 4\pi\rho_o r^2 G(r) = rT(r). \quad (2.12)$$

we can obtain the average number of neighboring atoms lying within the range of $(r, r + dr)$ from any given atom in a coordination shell by integrating $N(r)$:

$$n_{ij} = \frac{c_j}{W_{ij}} \int_{r_1}^{r_2} 4\pi\rho_o r^2 G(r) dr \quad (2.13)$$

and

$$n_{ij} = \frac{[c_O f_O(Q=0) + c_P f_P(Q=0) + c_R f_R(Q=0)]^2}{c_j f_i(Q=0) f_j(Q=0)} \int_{r_1}^{r_2} 4\pi\rho_o r^2 G(r) dr, \quad (2.14)$$

where n_{ij} is the coordination number. In this study, coordination numbers are calculated by fitting and integrating peaks in $G(r)$.

2.3 Preparation of REPGs

Samples were synthesized at the Physics & Astrophysics Department, University of North Dakota. Batched amounts of P_2O_5 , Na_2CO_3 and R_2O_3 were directly mixed in alumina crucibles and melted at $1300^\circ C$ for 1 hour in a high-temperature furnace. The melt was quenched in air in steel molds and, transferred to an annealing furnace as soon as it solidified. Quenched samples were annealed at $300^\circ C$ for approximately 1.5 hours.

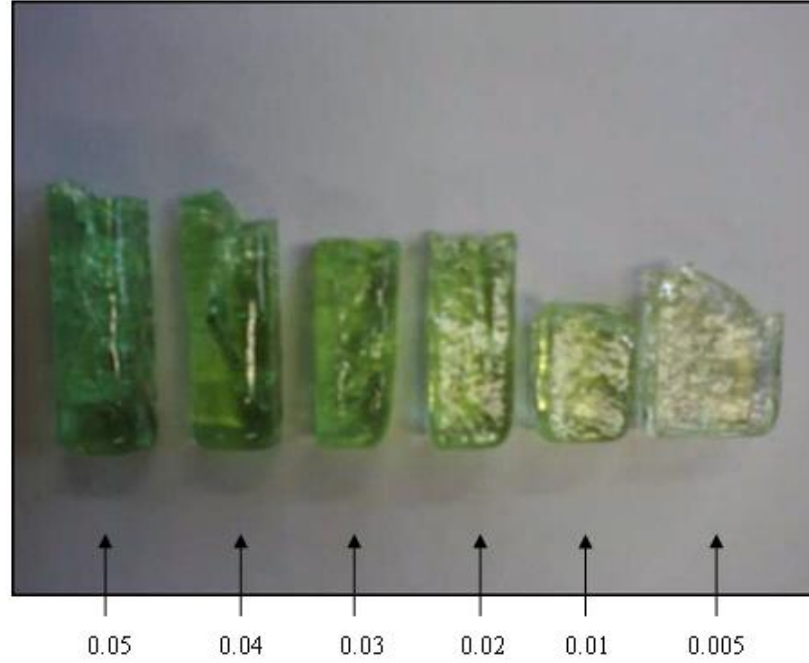


Figure 5. Praseodymium doped sodium phosphate glasses.

Table 3. Batched compositions and densities of $(Pr_2O_3)_x(Na_2O)_y(P_2O_5)_{1-x-y}$ glasses.

Sample ID	Composition of $Pr_2O_3(x)$	Composition of $Na_2O(y)$	Density (g/cm^3)	Number Density (Atoms/ \AA^3)
KZPr005	0.005	0.395	2.545	0.0745
KZPr010	0.010	0.390	2.578	0.0747
KZPr020	0.020	0.380	2.628	0.0747
KZPr030	0.030	0.370	2.716	0.0757
KZPr040	0.040	0.360	2.730	0.0747
KZPr050	0.050	0.350	2.794	0.0750

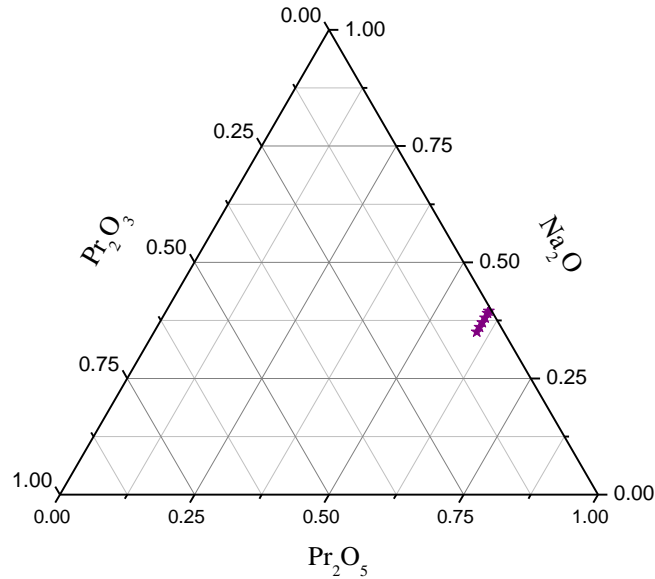


Figure 6. Ternary plot showing the batched composition of $(\text{Pr}_2\text{O}_3)_x(\text{Na}_2\text{O})_y(\text{P}_2\text{O}_5)_{1-x-y}$ glasses in this study.

2.4 Data Collection

Densities of the praseodymium doped sodium phosphate glasses were measured at the University of North Dakota using Archimedes method [4].

High energy X-ray diffraction measurements were carried out at beamline 11-ID- C at The Advanced Photon Source, Argonne National Laboratory, Chicago, IL. Measurements were done using synchrotron radiation of energy 115keV ($\lambda = 0.10801\text{\AA}$), flux of 10^{11} photons/second, and an unfocused beam of $0.2 \text{ mm} \times 0.2 \text{ mm}$ cross section. The sources of the high energy x-ray were undulators and data was collected by a large area detector.

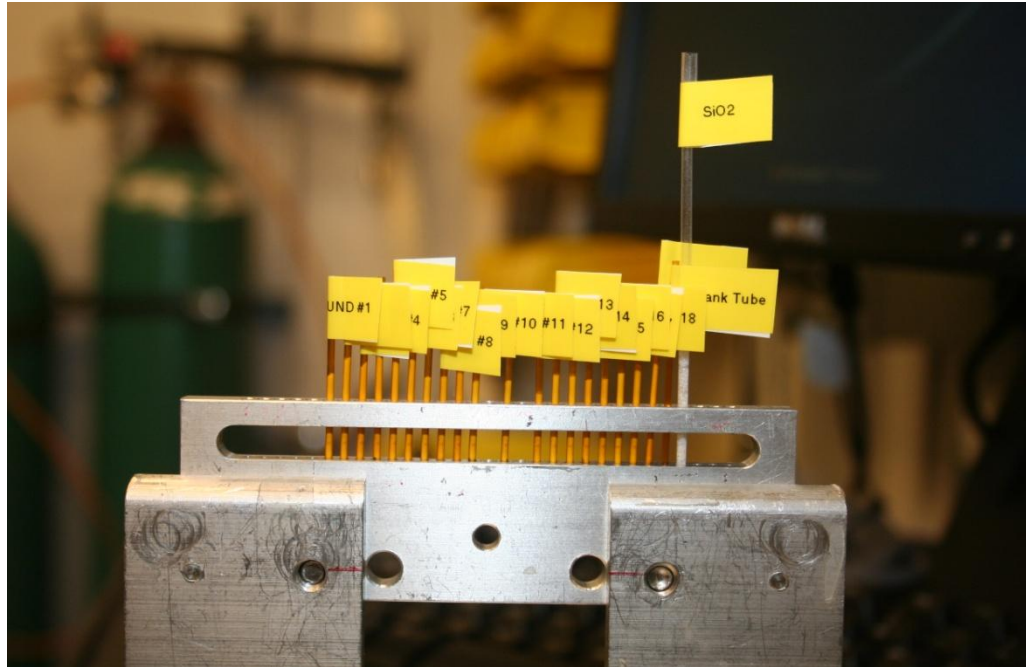


Figure 7. Polymide tubes containing powder samples. Tubes are of inner diameter 0.05” and outer diameter 0.054”.

Pr-Na-P-O samples were ground to (200 mesh) fine powders, and placed in polymide tubes, see Figure 6, for high-energy X-ray diffraction measurements. A labeled photograph and a sketch of the HEXRD setup are shown in Figure 7 and Figure 8, respectively. High-energy X-ray beam comes out of beam port, goes through a series of attenuators, collimators, diode and slits, and are diffracted from the sample. The 2D diffraction data was collected by a large area detector. The beam stop which was placed in the direct path of the beam, right in front of large area detector was used to prevent the direct beam from hitting the detector.

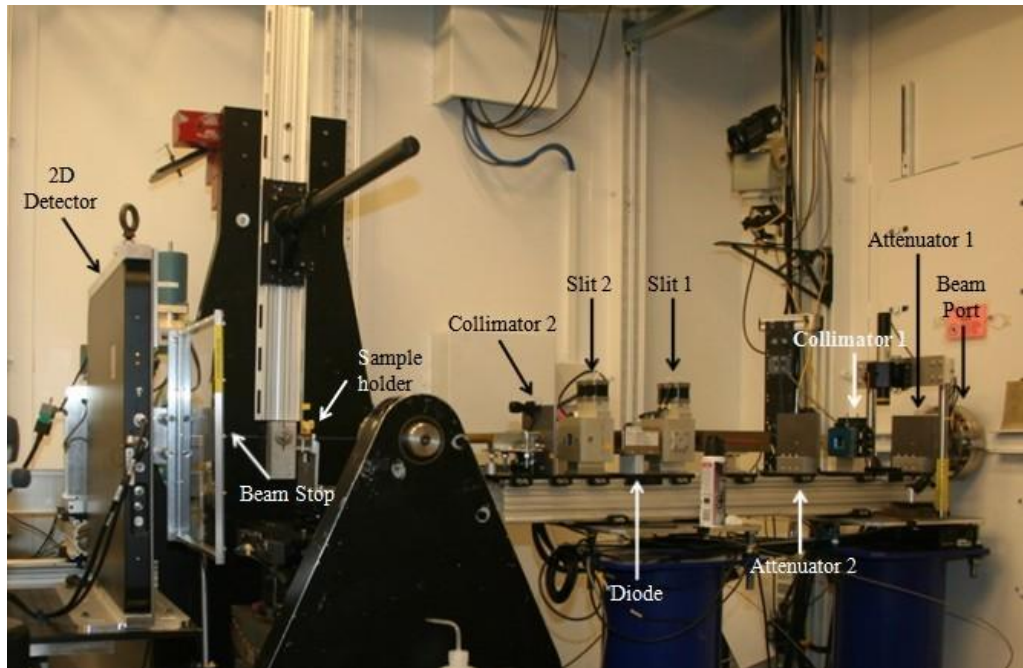


Figure 8. HEXRD setup at beamline 11-ID-C.

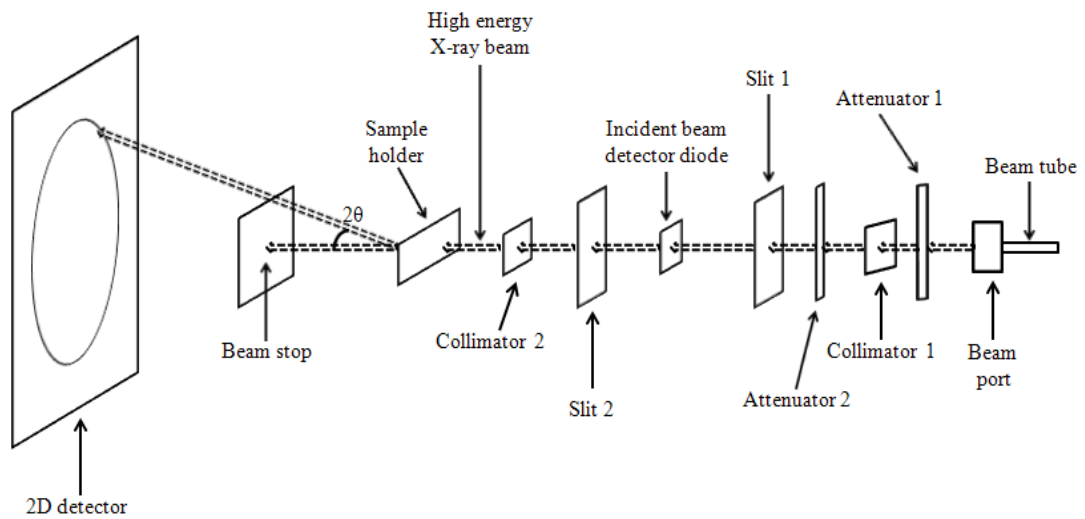


Figure 9. Sketch of the HEXRD experimental setup shown in Figure 8.

HEXRD data was collected for a crystalline CeO_2 standard, an empty sample tube, an empty specimen slot (scattering from air), a crystalline SiO_2 sample and for the six

glass samples. Twenty data sets were collected for each of the samples, ten each at sample to detector distances of 380mm and 420mm.

Emission spectra of praseodymium-doped sodium phosphate glasses were measured at the Department of Material Science and Engineering, Missouri University of Science and Technology, Rolla, Missouri.

2.5 Methods of HEXRD Data Analysis

In this work, data sets which were collected at the sample to detector distance of 380 mm were analyzed. Fit2D program [4] was used to process the two-dimensional diffraction patterns obtained. Fit2D first averages the ten runs (averaged diffraction pattern shown in Figure 9), and outputs intensity versus 2θ data by integrating the two-dimensional data. Figure 10 shows how Fit2D program works. Input of Fit2D is a .tiff file and its output a .chi file.

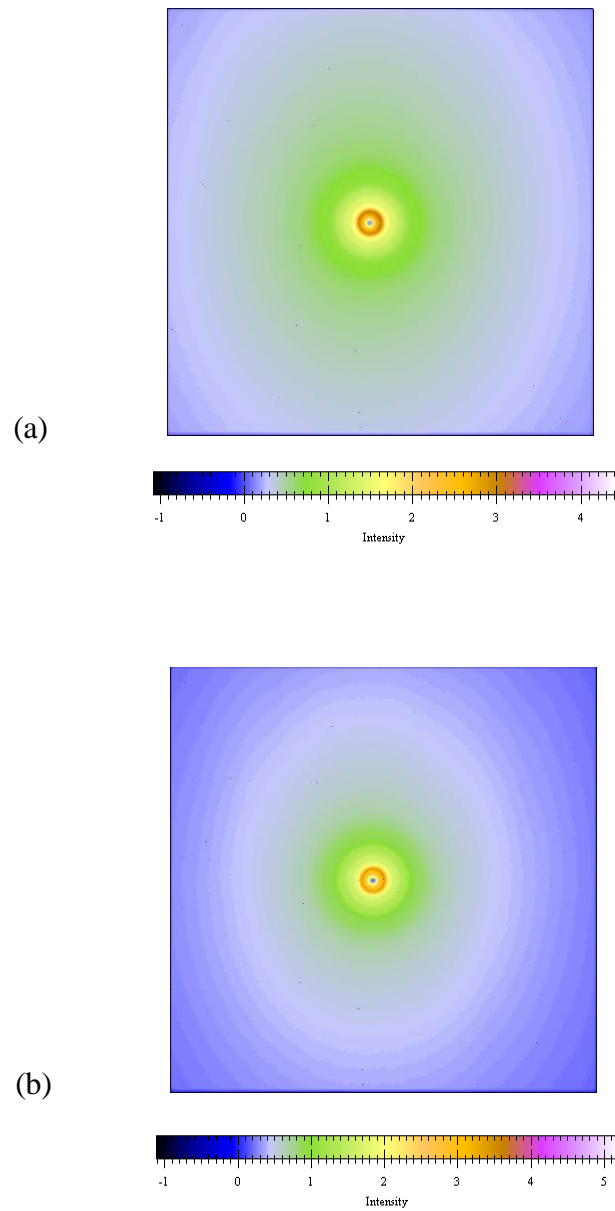


Figure 10. Averaged 2D high energy X-ray diffraction patterns for (a) $(\text{Pr}_2\text{O}_3)_{0.005}(\text{Na}_2\text{O})_{0.395}(\text{P}_2\text{O}_5)_{0.6}$ (b) $(\text{Pr}_2\text{O}_3)_{0.01}(\text{Na}_2\text{O})_{0.39}(\text{P}_2\text{O}_5)_{0.6}$.

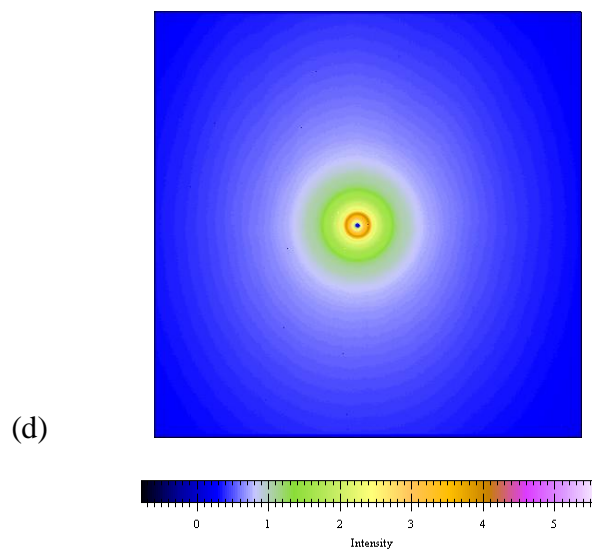
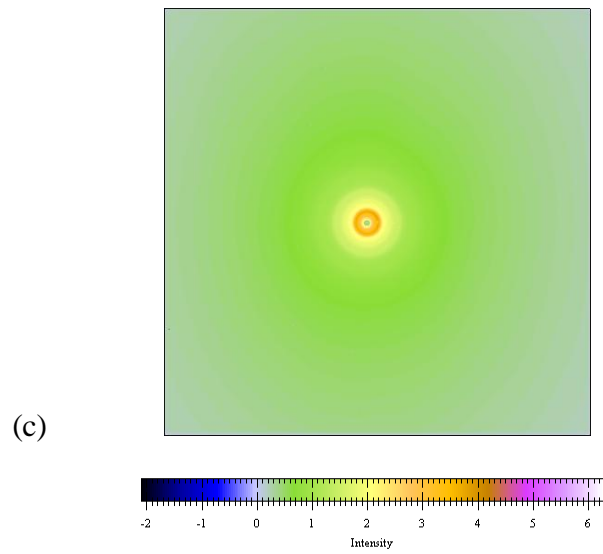


Figure 11. Averaged 2D high energy X-ray diffraction patterns for (c) $(\text{Pr}_2\text{O}_3)_{0.02}(\text{Na}_2\text{O})_{0.38}(\text{P}_2\text{O}_5)_{0.6}$ (d) $(\text{Pr}_2\text{O}_3)_{0.03}(\text{Na}_2\text{O})_{0.37}(\text{P}_2\text{O}_5)_{0.6}$.

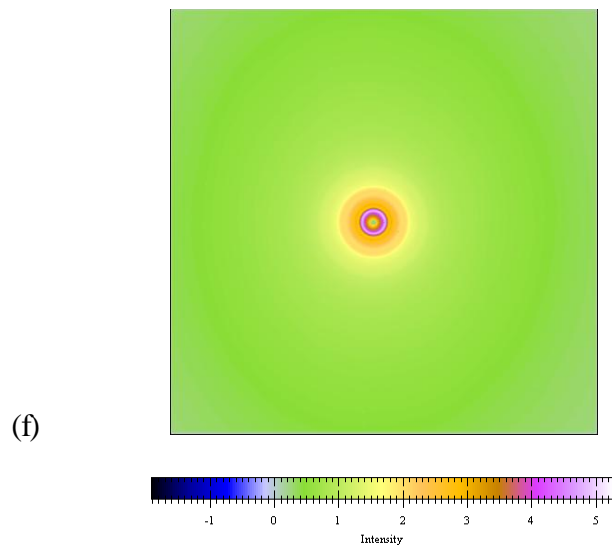
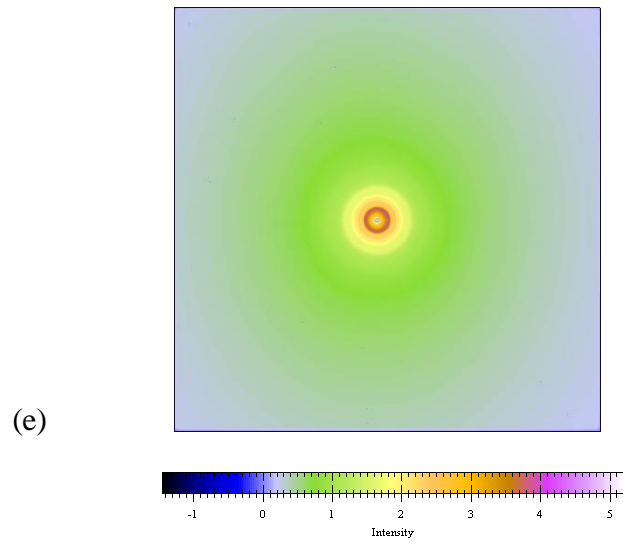


Figure 12. Averaged 2D high energy X-ray diffraction patterns for (e) $(\text{Pr}_2\text{O}_3)_{0.04}(\text{Na}_2\text{O})_{0.36}(\text{P}_2\text{O}_5)_{0.6}$ (f) $(\text{Pr}_2\text{O}_3)_{0.05}(\text{Na}_2\text{O})_{0.35}(\text{P}_2\text{O}_5)_{0.6}$.

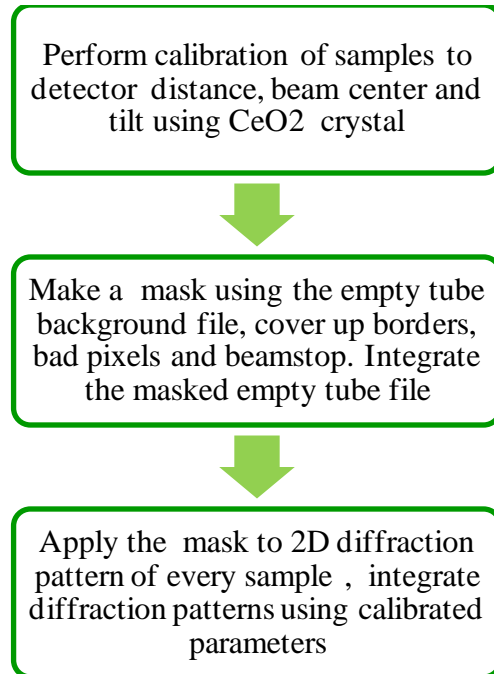


Figure 13. Flow chart for Fit-2D program.

Integrated intensities were then corrected for unwanted effects (see next paragraph) to obtain structure factors $S(Q)$, which were Fourier transformed to get the pair distribution function $G(r)$ (equation 2.7). This process was done using PDFgetX2 program [15] [16].

Attenuation of high-energy X-rays and multiple scattering is relatively low and doesn't pose too much of a problem. However, Compton (inelastic) scattering can be very strong, especially at high Q values, and should be carefully eliminated from the measured data. Fluorescence energies of elements in the sample were subtracted. Scattering from the sample holder (empty tube) and the background (scattering from air) was also subtracted from the measured intensity before being converted to $S(Q)$.

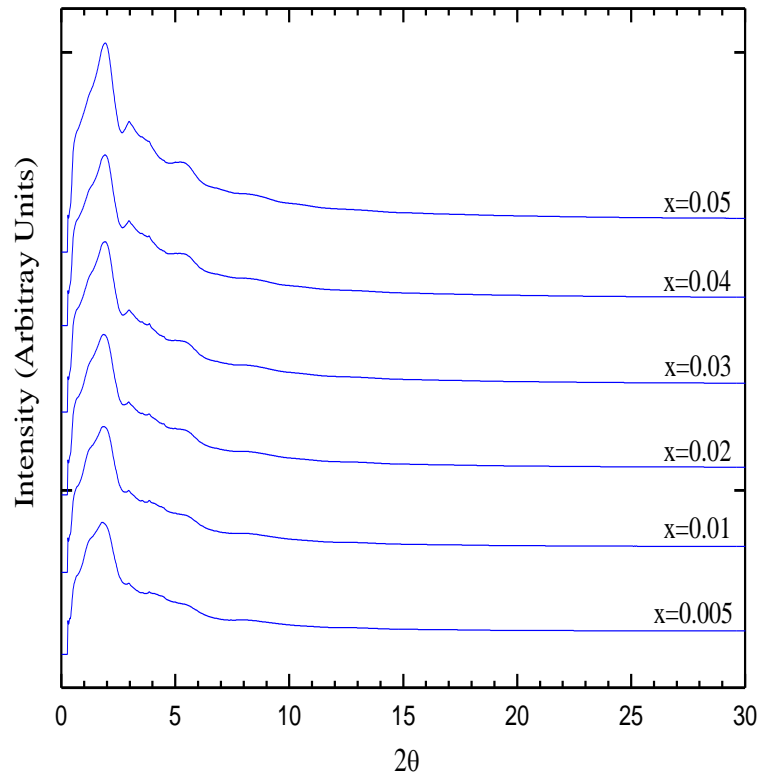


Figure 14. Intensity vs. 2θ plots for $(\text{Pr}_2\text{O}_3)_x(\text{Na}_2\text{O})_y(\text{P}_2\text{O}_5)_{1-x-y}$ glasses. Absence of sharp Bragg diffraction peaks indicates the lack of long-range periodicity in the structure of glass samples.

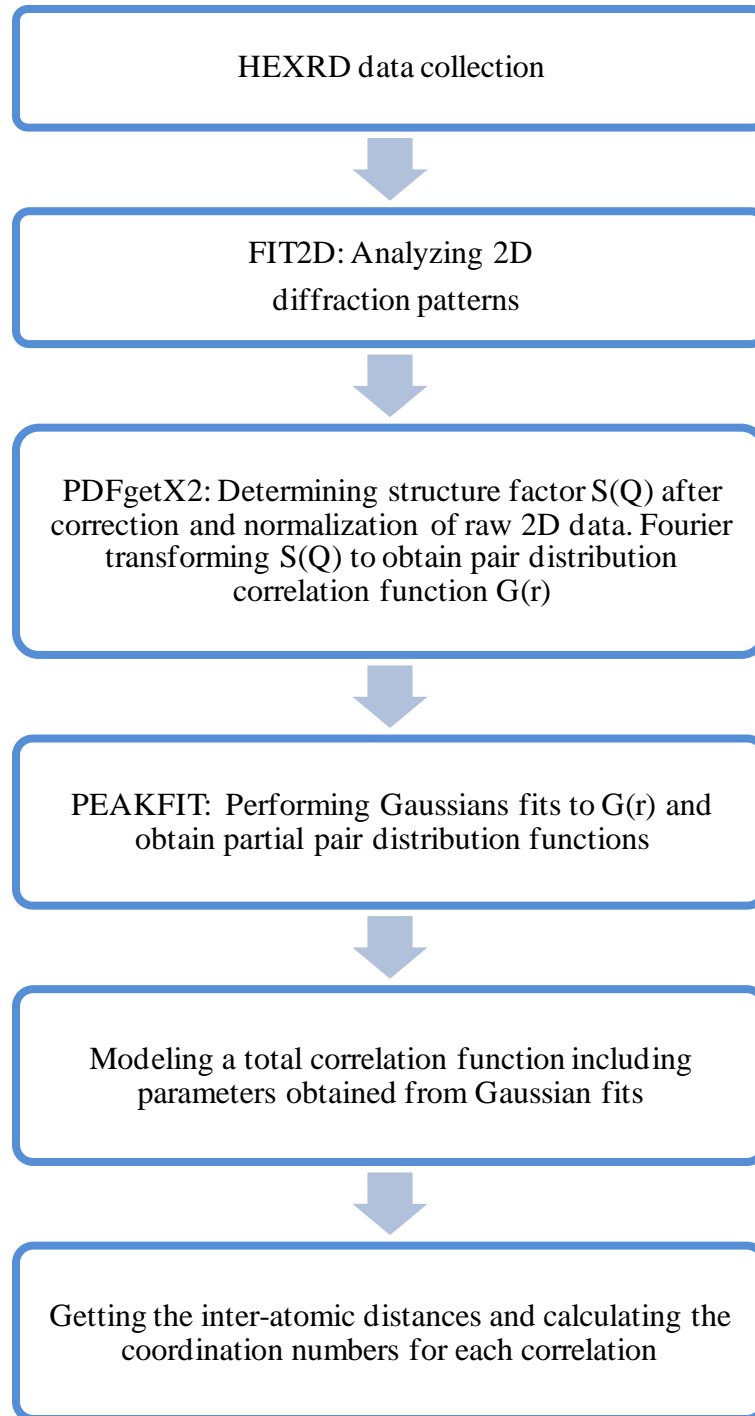


Figure 15. Flow chart for the analysis of HEXRD data for praseodymium-doped sodium phosphate glasses.

$G(r)$ functions were used to extract information such as bond distances, local coordination numbers, average bond angles [12], etc. It describes the probability of finding any two atoms at given inter-atomic distances. Atomic structural information relevant to P-O, Pr-O, O-O, P-P and Na-O correlations were obtained by fitting $G(r)$ with Gaussians. The area under each Gaussian peak is proportional to the coordination numbers of correlation represented by that peak.

CHAPTER III

RESULTS AND DISCUSSION

3.1 Results

As seen in Figure 13, the density of praseodymium-doped sodium phosphate glasses increases almost linearly with Pr_2O_3 concentration.

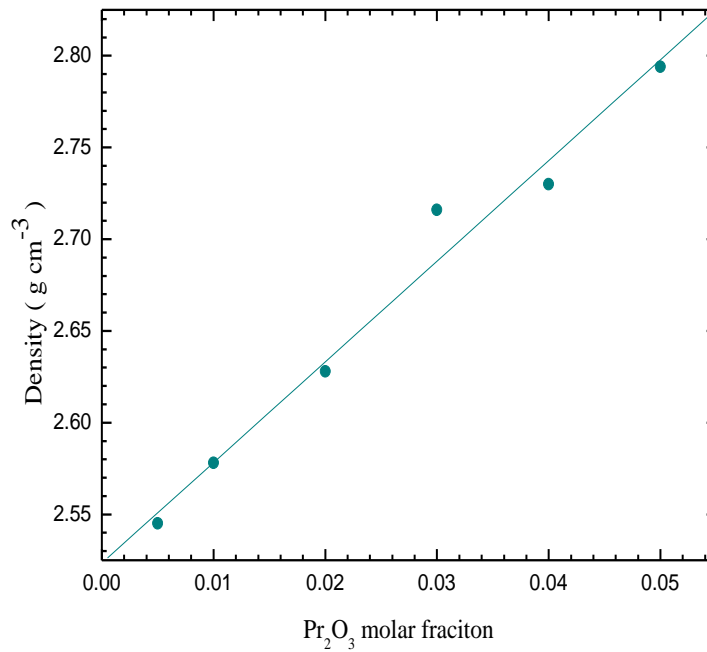


Figure 16. Dependence of mass density on rare earth oxide content for $(\text{Pr}_2\text{O}_3)_x(\text{Na}_2\text{O})_y(\text{P}_2\text{O}_5)_{1-x-y}$ glasses.

X-ray structure factors $S(Q)$ extracted from the HEXRD data are shown in Figure 17. Even though data was collected up to a maximum Q value of $\sim 30.1 \text{ \AA}^{-1}$, Figure 14 shows $S(Q)$ only up to 25 \AA^{-1} .

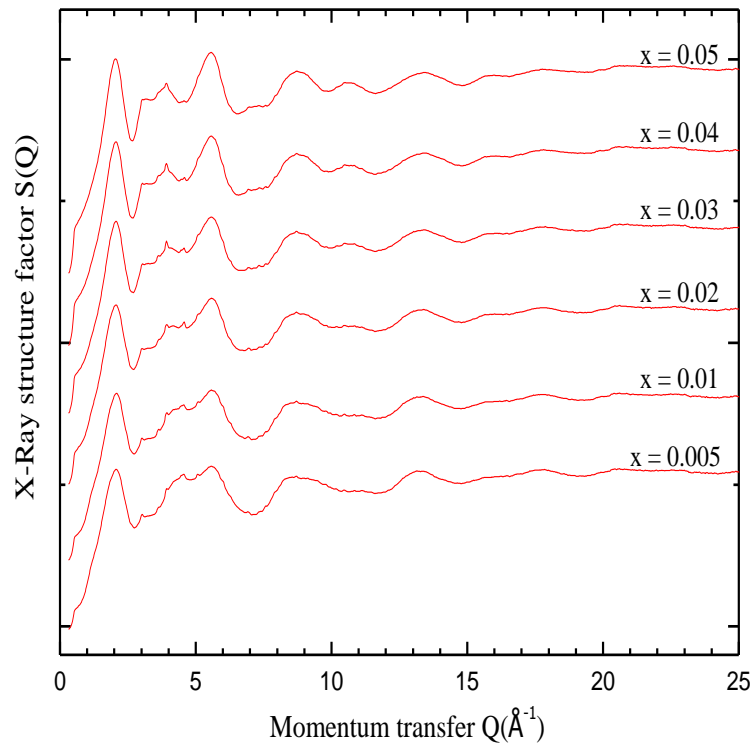


Figure 17. X-ray structure factors, $S(Q)$, for $(\text{Pr}_2\text{O}_3)_x(\text{Na}_2\text{O})_y(\text{P}_2\text{O}_5)_{1-x-y}$ glasses. Successive plots are shifted vertically for clarity.

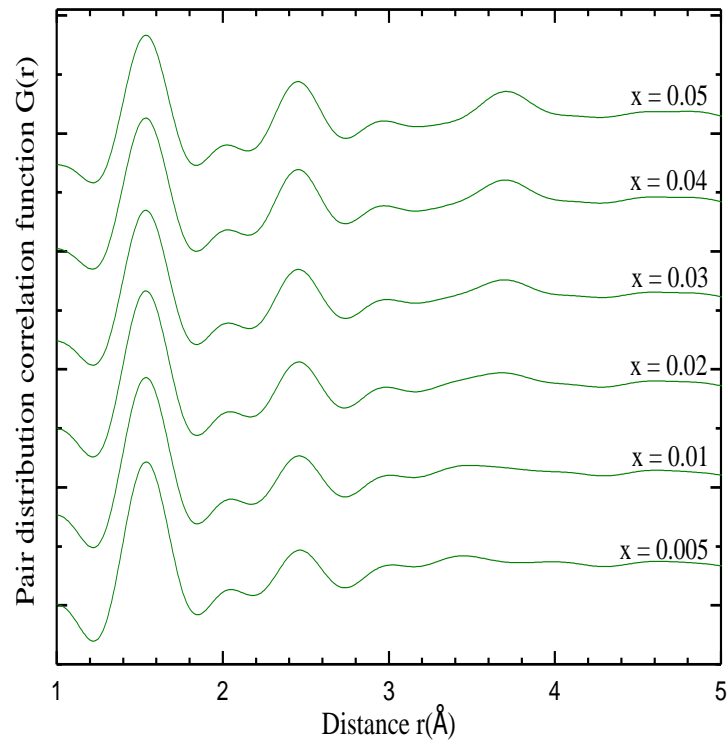


Figure 18. Pair distribution function $G(r)$ for $(\text{Pr}_2\text{O}_3)_x(\text{Na}_2\text{O})_y(\text{P}_2\text{O}_5)_{1-x-y}$ glasses. Successive plots are shifted vertically for clarity.

$S(Q)$ was cut off at $Q \sim 16.7 \text{ \AA}^{-1}$ when Fourier transforming to get $G(r)$ which are shown in Figure 18. Pair distribution functions shown in Figure 18 were fitted with Gaussians. Figure 19 shows $G(r)$ of $(\text{Pr}_2\text{O}_3)_{0.05}(\text{Na}_2\text{O})_{0.35}(\text{P}_2\text{O}_5)_{0.6}$ glasses fitted with Gaussians.

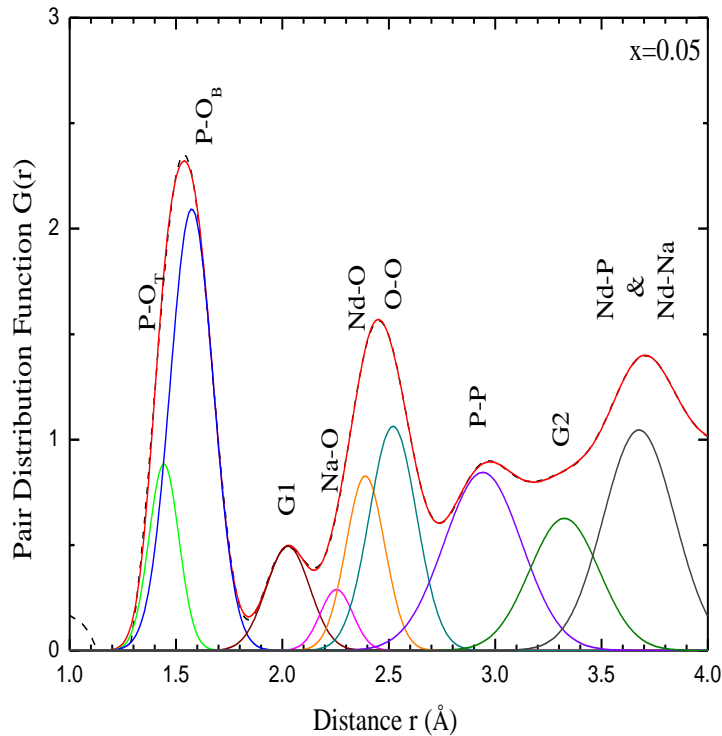


Figure 19. $G(r)$ for $(\text{Pr}_2\text{O}_3)_{0.05}(\text{Na}_2\text{O})_{0.35}(\text{P}_2\text{O}_5)_{0.6}$ glasses (dotted line) fitted with Gaussians. Red line is the overall fit, individual Gaussians represent different pair correlations.

A Gaussian labeled A-B represents correlations between atoms A and B. Assuming praseodymium (59) and neodymium (60), which are neighbors in the periodic table, wouldn't make too much difference in the structure of glass samples, the experimental $G(r)$ of Pr-Na-P-O glasses are mostly fitted based on the known structure of $\text{NdNaP}_4\text{O}_{12}$ crystal (Figure 20).

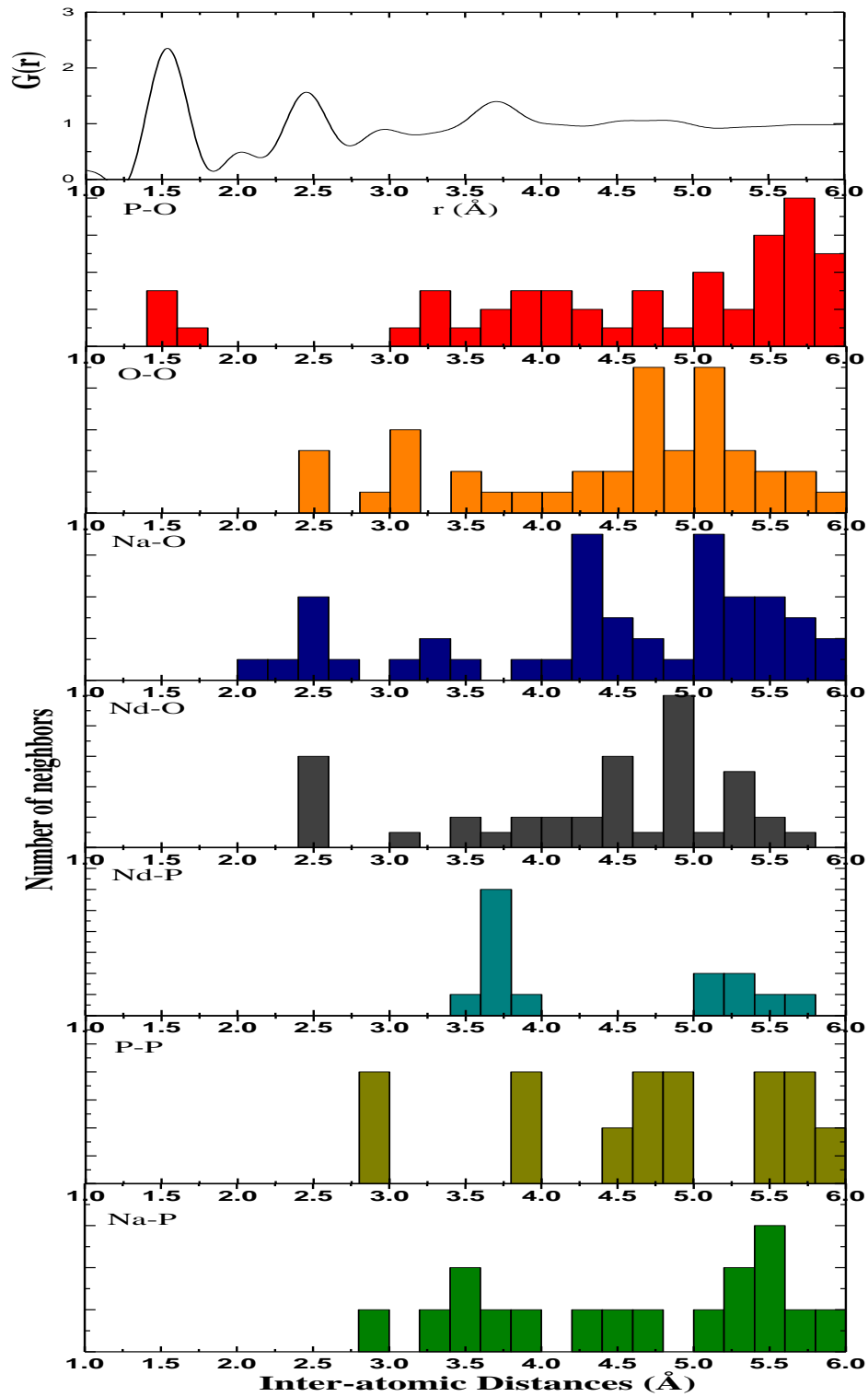


Figure 20. Comparison of $G(r)$ for KZPr50 glass sample with inter-atomic distance distribution of crystalline $\text{NdNaP}_4\text{O}_{12}$ [4].

The first peak of $G(r)$ at $\sim 1.5 \text{ \AA}$ represents P-O correlations. It was fitted with two Gaussians, one corresponding to P-O_T (terminal oxygen) correlations and the other one corresponding to P-O_B (bridging oxygen) correlations. Average P-O distance is ~ 1.51 , coordination number ~ 3.44 . Pr-O mean distance is $\sim 2.4 \text{ \AA}$. The coordination number of N_{PrO} ranges from ~ 8.3 to 11.4 . It decreases with increasing rare earth content. Average Na-O distance for praseodymium sodium phosphate glasses is $\sim 2.3 \text{ \AA}$. The coordination number varies from ~ 1.02 to 2.37 . Mean P-P distance of $(\text{Pr}_2\text{O}_3)_x(\text{Na}_2\text{O})_y(\text{P}_2\text{O}_5)_{1-x-y}$ is approximately 2.93 \AA . Emission spectra of Pr-Na-P-O glasses with various Pr_2O_3 concentrations are shown in Figure 21. The peak observed at $\sim 640\text{nm}$ corresponds to ${}^3\text{P}_0 \rightarrow {}^3\text{F}_2$ transition of Pr^{3+} (Figure 1.)

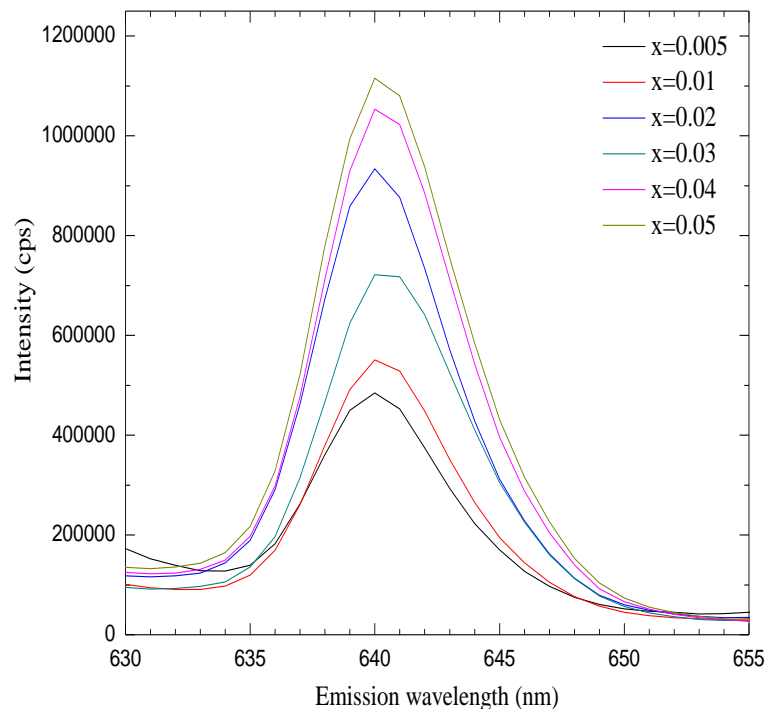


Figure 21. Emission spectra of Pr-Na-P-O glasses with different praseodymium concentrations.

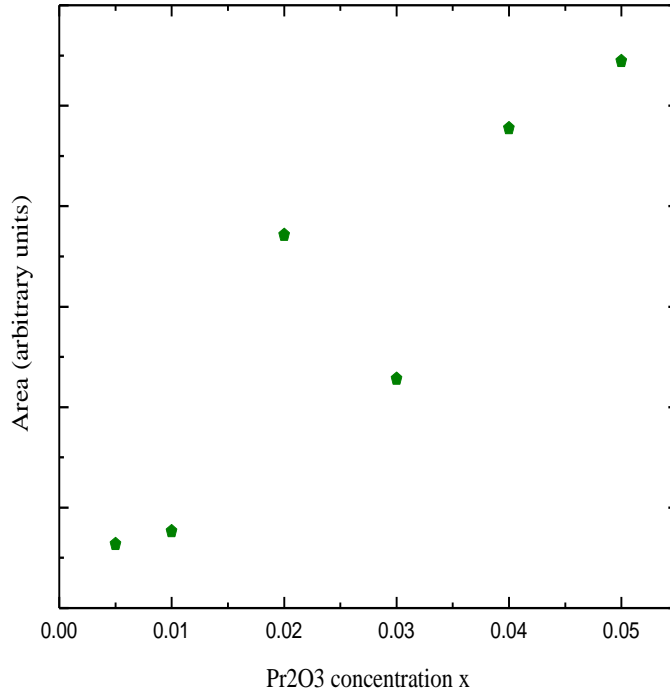


Figure 22. Integrated area of the emission line at ~640 nm vs. x for $(\text{Pr}_2\text{O}_3)_x(\text{Na}_2\text{O})_y(\text{P}_2\text{O}_5)_{1-x-y}$ glasses. Except for the two samples with $x=0.02$ and 0.03 , emission efficiency appear to decrease with decreasing Pr^{3+} concentration.

The integrated area under emission spectra shown in Figure 21 vs. molar fraction of Pr_2O_3 x is plotted in Figure 22. For $x = 0.005, 0.01, 0.04, 0.05$, as Pr_2O_3 concentration increases, the fluorescence intensity increases accordingly. This behavior is in contrast to that observed in rare earth-doped phosphate glasses having higher rare earth concentrations ($x \geq 0.05$) including a series of Nd^{3+} glasses studied by our group, see Figures 2 and 3. Data for $x = 0.02$ and 0.03 samples, however, do not fit the trend shown in Figure 22.

Table 4. Coordination numbers N_{ij} and inter-atomic distances r_{ij} (Å) of $(\text{Pr}_2\text{O}_3)_x(\text{Na}_2\text{O})_y(\text{P}_2\text{O}_5)_{1-x-y}$ glasses obtained by fitting $G(r)$ s. All inter-atomic distances are in Angstroms.

Sample ID	x	y	N_{POT}	r_{POT}	N_{POB}	r_{POB}	$N_{\text{PO(Total)}}$	$r_{\text{PO(Avg.)}}$	N_{NiO}	r_{NiO}	N_{PrO}	r_{PrO}	N_{OO}	r_{OO}	r_{PP}
KZPr005	0.005	0.395	0.72	1.45	2.74	1.58	3.461	1.85	2.37	2.34	11.37	2.45	4.79	2.52	2.93
KZPr010	0.01	0.39	0.7	1.44	2.69	1.58	3.395	1.51	1.25	2.31	11.19	2.43	5.44	2.52	2.93
KZPr020	0.02	0.38	0.72	1.44	2.74	1.58	3.454	1.51	1.02	2.26	9.02	2.39	5.45	2.52	2.92
KZPr030	0.03	0.37	0.7	1.44	2.74	1.58	3.441	1.51	1.3	2.26	8.71	2.39	4.75	2.52	2.96
KZPr040	0.04	0.36	0.64	1.44	2.73	1.57	3.367	1.505	1.36	2.24	8.27	2.38	4.98	2.52	2.94
KZPr050	0.05	0.35	0.67	1.44	2.81	1.57	3.486	1.505	1.4	2.25	6.95	2.39	5.1	2.52	2.94

3.2 Discussion

As seen in Figure 13, mass densities of Pr-Na-P-O glasses increase almost linearly with the Pr_2O_3 content. This can be attributed to the increasing amount of the heavy rare-earth ions. Calculated slope for this dependence is 5.49 g cm^{-3} per x .

In the intensity vs. 2θ data (Figure 14) for Pr-Na-P-O glasses, KZPr050 ($x = 0.05$) sample has a rather obvious peak at $2\theta \sim 3^\circ$. This is quite likely due to a crystalline component of this particular sample. As the rare earth concentration decreases, this crystalline peak becomes almost absent.

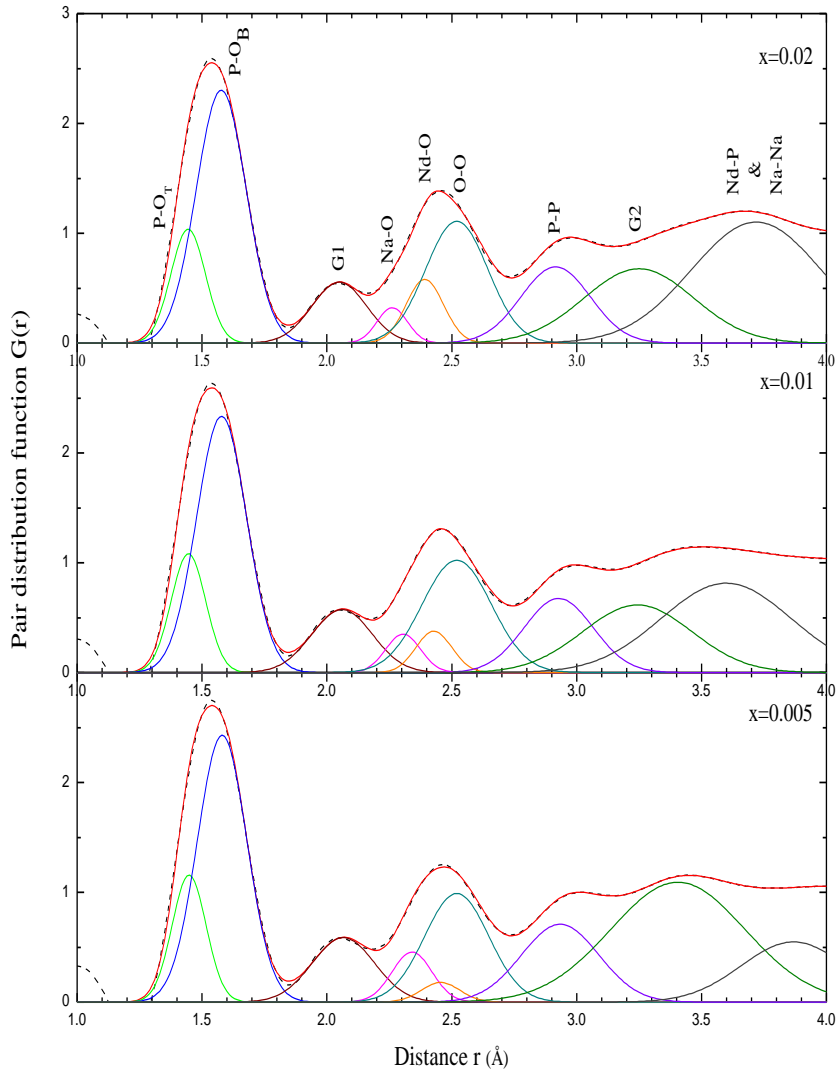


Figure 23. $G(r)$ for $(Pr_2O_3)_x(Na_2O)_y(P_2O_5)_{1-x-y}$ glasses (dotted line) with $x=0.005, 0.01, 0.02$ fitted with Gaussians. Red line is the overall fit, individual Gaussians represent different pair correlations.

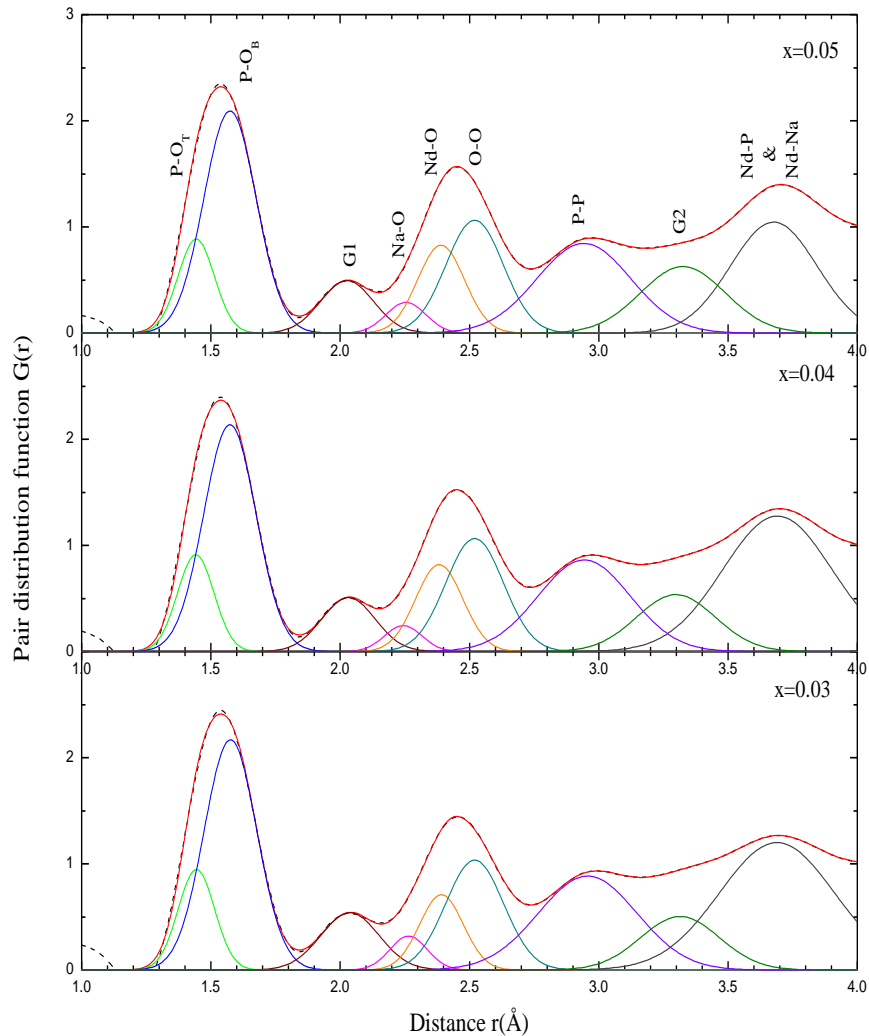


Figure 24. $G(r)$ for $(\text{Pr}_2\text{O}_3)_x(\text{Na}_2\text{O})_y(\text{P}_2\text{O}_5)_{1-x-y}$ glasses (dotted line) with $x=0.03, 0.04, 0.05$ fitted with Gaussians. Red line is the overall fit, individual Gaussians represent different pair correlations.

The average coordination number of P-O correlation is ~ 3.4 , slightly less than the expected 4, but nevertheless underscores the presence of $(\text{PO}_4)^{3-}$ tetrahedra units in the glass samples examined. The $(\text{PO}_4)^{3-}$ units have one shorter P-O_T bond, and three longer P-O_B bonds, hence P-O_T correlation was fitted at $\sim 1.44 \text{ \AA}$ with smaller Gaussians, and P-

O_B correlation at $\sim 1.58\text{\AA}$ with bigger Gaussians. The P-O coordination number and the mean distances for P-O pairs do not change apparently with the Pr_2O_3 concentration, in agreement with several phosphate systems investigated in previous studies [15] [16] [17] [18]. A Gaussian fixed at 2.52\AA is used to represent O-O correlations. The rest of the Gaussians representing correlations such as Na-O, Pr-O were added based on the crystal structure of $\text{NdNaP}_4\text{O}_{12}$, as we expect the short-range structures of the glass and the crystal to be similar. The peak preceding the Na-O peak is not related to any correlations. This peak is assumed to be a result of the relatively severe Fourier series termination ripples in the low- r region.

Since there is not enough information about the structure of praseodymium doped sodium phosphate glasses, it is impractical to fix any parameters of the Gaussians fitted for the peak at $r \sim 2.5\text{\AA}$ (Na-O, Pr-O, O-O) except for the distance of O-O correlation (fixed at 2.52\AA). Parameters obtained for these Gaussians can have considerable uncertainties.

The coordination number of Pr-O correlation at $r \sim 2.4\text{\AA}$ is rather large at $x = 0.005$ & 0.01 , and it decreases with increasing rare earth concentration. This could be explained by the fact that when the rare-earth concentration increases, more bridging oxygens have to bond with the modifying rare-earth ions. Thus fewer bridging oxygens become available to be converted to terminal oxygens, resulting in a decrease of the R-O coordination numbers.

The third peak of $G(r)$ centered at around 2.9\AA includes Na-P and P-P correlations. Since the distance of these two correlations are very similar and the P-P correlation is more dominant, it is difficult to separate the two Gaussians. In this study,

only the distance of P-P correlation is considered and not the Na-P coordination number. The near-neighbor P-P distance is $\sim 2.93 \text{ \AA}$. The fourth peak at $\sim 3.7 \text{ \AA}$ is due to Nd-P and Nd-Na correlations. At this distance the second coordination shells of P-O, O-O, Na-O and Na-P overlap and make it difficult to differentiate the Gaussians. Due to this the coordination numbers for Nd-P and Nd-Na were not calculated.

It can be seen from Fig. 18 that the integrated area of peaks at $\sim 2.5 \text{ \AA}$ and $\sim 3.9 \text{ \AA}$ decrease with decreasing Pr_2O_3 concentration, more so for the peak at $\sim 3.9 \text{ \AA}$. When $x = 0.005$, the peak at $\sim 3.9 \text{ \AA}$ becomes almost inconspicuous.

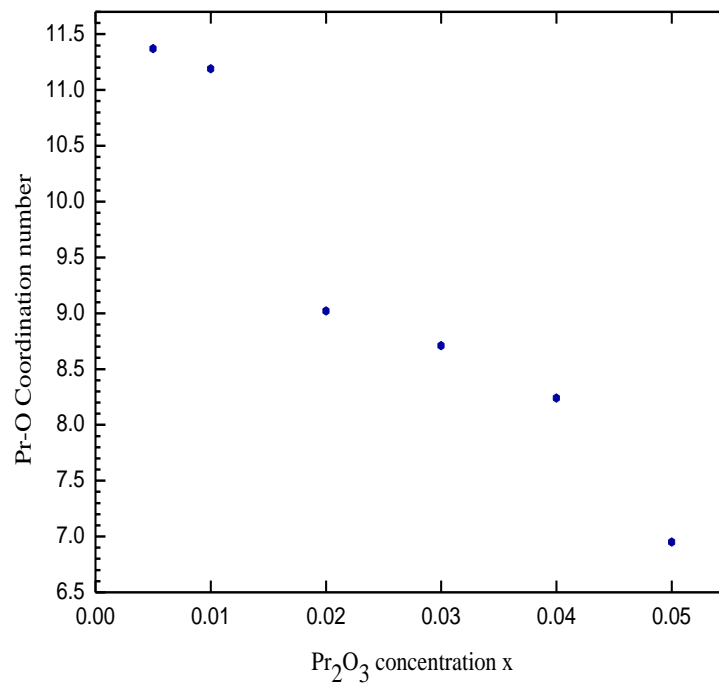


Figure 25. The effect of composition on the Pr-O coordination number for $(\text{Pr}_2\text{O}_3)_x(\text{Na}_2\text{O})_y(\text{P}_2\text{O}_5)_{1-x-y}$ glasses.

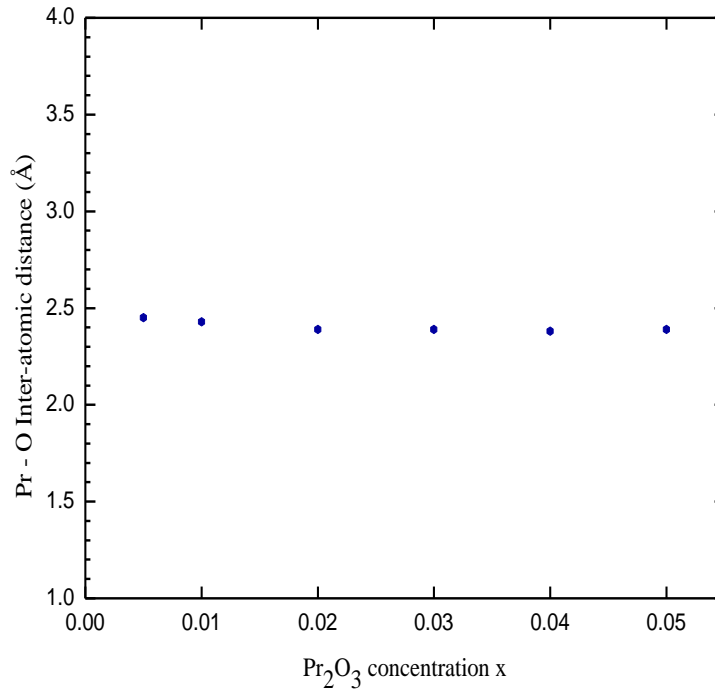


Figure 26. The effect of composition on the Pr-O inter-atomic distances for $(\text{Pr}_2\text{O}_3)_x(\text{Na}_2\text{O})_y(\text{P}_2\text{O}_5)_{1-x-y}$ glasses.

Figure 27 compares the plot of integrated area of the emission line at ~ 1050 nm vs. x of $(\text{Nd}_2\text{O}_3)_x(\text{Na}_2\text{O})_y(\text{P}_2\text{O}_5)_{1-x-y}$ glasses investigated in prior work by our group [4] and the data for $(\text{Pr}_2\text{O}_3)_x(\text{Na}_2\text{O})_y(\text{P}_2\text{O}_5)_{1-x-y}$ glasses shown in Figure 22. For $(\text{Pr}_2\text{O}_3)_x(\text{Na}_2\text{O})_y(\text{P}_2\text{O}_5)_{1-x-y}$ glasses in the range of $0.005 < x < 0.05$, the fluorescence intensity generally increase as the Pr_2O_3 concentration increases. For $(\text{Nd}_2\text{O}_3)_x(\text{Na}_2\text{O})_y(\text{P}_2\text{O}_5)_{1-x-y}$, in the range of $0.04 < x < 0.12$, the fluorescence intensity decrease as the Nd_2O_3 concentration increase. Noting that Pr and Nd are neighboring rare earths and, as a result, one can reasonably expect similarities in structural and optical

properties of these two families of glasses, it appears that the optimum R^{3+} concentration is in the $x = 0.04-0.05$ range. Although there is inconsistency of the data in

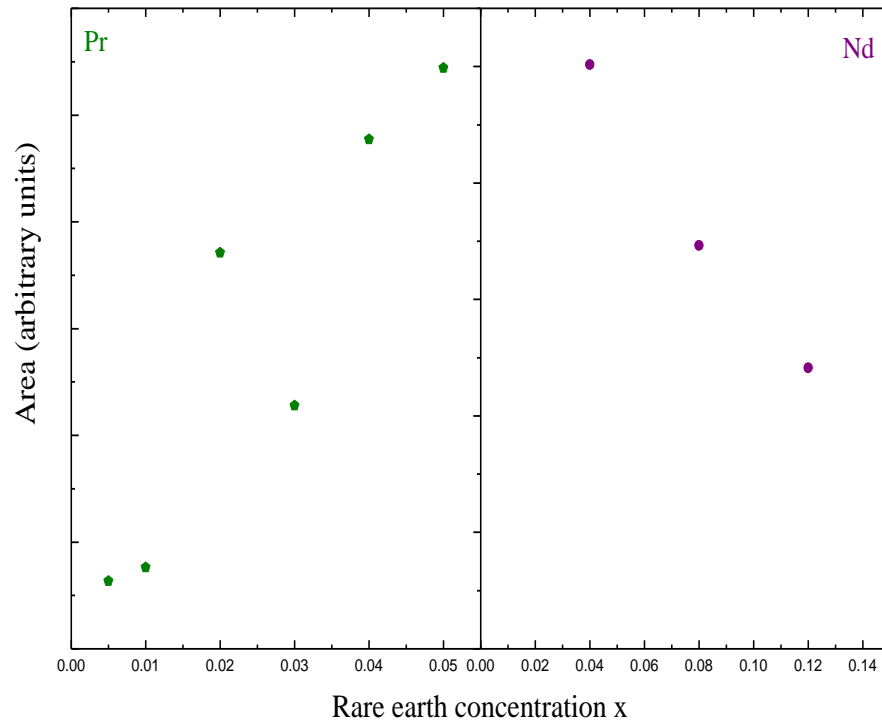


Figure 27. Integrated area of selected emission lines vs. x for $(Pr_2O_3)_x(Na_2O)_y(P_2O_5)_{1-x-y}$ (left) and $(Nd_2O_3)_x(Na_2O)_y(P_2O_5)_{1-x-y}$ (right) glasses.

$(Pr_2O_3)_x(Na_2O)_y(P_2O_5)_{1-x-y}$ glasses at $x = 0.02$ and 0.03 , for now I can cautiously draw the conclusion that the lasing ability of rare earth sodium phosphate glasses peak when rare earth oxide concentration $x = 0.05$. Further measurements need to be taken to verify and confirm this conclusion.

CHAPTER IV

CONCLUSION

The atomic-scale structure of $(\text{Pr}_2\text{O}_3)_x(\text{Na}_2\text{O})_y(\text{P}_2\text{O}_5)_{1-x}$ glasses of low praseodymium oxide concentration, where $0.005 < x < 0.05$ has been studied using the high-energy X-ray diffraction technique. First neighbor inter-atomic distances, coordination numbers and their dependence on the concentration of the praseodymium oxide have been obtained by analyzing pair distribution functions extracted from HEXRD data.

Average P-O, Pr-O, P-P first coordination shell distances for $(\text{Pr}_2\text{O}_3)_x(\text{Na}_2\text{O})_y(\text{P}_2\text{O}_5)_{1-x}$ are 1.51, 2.4, 2.94 Å respectively, and are independent of the Pr_2O_3 concentration. Average P-O coordination number is about 3.4, smaller than the expected 4, and also independent of Pr_2O_3 concentration. The coordination number of Pr-O ranges from ~ 8.3 to ~ 11.4 , decreases with increasing rare earth content. This is likely due to the fact that when the rare-earth concentration increases, more bridging oxygens have to bond with the modifying rare-earth ions. Thus fewer bridging oxygens become available to be converted to terminal oxygens, result in a decrease of the Pr-O coordination numbers.

The emission characteristic studies of praseodymium doped sodium phosphate glasses suggest that there is a directly proportional correlation between Pr_2O_3 concentration and the emission intensity. Combined with the emission spectra of

neodymium doped sodium phosphate glasses previously observed, I cautiously drew the conclusion that the lasing ability of rare earth sodium phosphate glasses peak when rare earth oxide concentration $x = 0.05$. Further emission spectroscopy studies are needed to confirm this conclusion.

REFERENCES

- [1] Rudiger Paschotta, Encyclopedia of laser physics and technology. Vch Pub, 2008.
- [2] Hucheng Yang, Jianrong Qiu G.Lakshminarayana, Photoluminescence of Pr³⁺-, Nd³⁺- and Ni²⁺- doped TeO₂-ZnO-WO₃-TiO₂-Na₂O glasses, Journal of Alloys and Compounds, 475 (2009).
- [3] John D. Myers, Michael J. Myers Ruikun Wu, New generation high power rare-earth-doped phosphate glass fiber and fiber laser. Photonics West, 2001.
- [4] Erandi S. Gunapala, A study of the atomic structure of vitreous rare earth phosphates using high energy X-ray diffraction technique. University of North Dakota, 2011.
- [5] R. K. Brow, J. Non-Cryst. Solids 263&264 (2000) 1.
- [6] G. K. Marasinghe, E. Metwalli, R. K. Brow, C. H. Booth, J. J. Bucher, D. K. Shuh M. Karabulut, J. Non-Cryst. Solids 351 (2005) 795.
- [7] R. J. Newport J. M. Cole, J. Non-Cryst. Solids 353 (2007) 1773.
- [8] Yuanbing Mao, John Bargar, Michael Toney, Jane P. Chang, Correlation between luminescent properties and local coordination environment for erbium dopant in yttrium oxide nanotubes, Journal of Applied Physics, 103 (2008) 9.
- [9] S. Todoroki, N. Soga K. Hirao, J. Non-Cryst. Solids 175 (1994) 263.
- [10] Valeri Petkov, Nanostructure by high-energy X-ray diffraction, Materials Today, 11 (2008) 11.
- [11] Simon J. L. Billinge, The atomic pair distribution function: past and present, Z. Kristallogr. 219 (2004) 117-121.
- [12] Chris Benmore, High energy X-ray diffraction from liquids and glasses. Argonne National Lab.
- [13] H. F. Poulsen, J. Neufeind, H. B. Neumann, J. R. Schneider, M. D. Zeidler,

Amorphous silica studied by high energy x-ray diffraction. Journal of Non-Crystalline Solids, 188 (1995) 63-74.

- [14] S Kohara, M Itou, K Suzuya, Y Inamura, Y Sakurai, Y Ohishi, M Takata, Structural studies of disordered materials using high energy x-ray diffraction. Journal of Physcs: Condensed Matter, 19 (2007) 50.
- [15] Chris Benmore, Pair distribution function analysis. X-ray Science Division, Argonne National Lab.
- [16] Simon Billinge, Xiangyun Qiu, PDFgetX2 manual. East Lansing, Michigan, USA, 2004.
- [17] G. Walter, D. Stachel U. Hoppe, Silikattechnik, 41 (1990) 227.
- [18] G. Walter, R. Kranold, D. Stachel, A. Barz U. Hoppe, J. Non-Cryst. Solids, 192&193 (1995) 28.
- [19] G. Walter, D. Stachel, A. Barz, A.C.Hannon U. Hoppe, Z. Naturforsch. A, 52 (1997) 259.
- [20] R. Kranold, D. Stachel, A. Barz, A. C. Hannon U. Hoppe, Z. Naturforsch. A, 55 (2000) 369.